Journal of Solid State Electrochemistry (2024) 28:829–845
https://doi.org/10.1007/s10008-023-05770-w

REVIEW PAPER

Electrochemistry and band structure of semiconductors (TiO_2, SnO_2, ZnO): Avoiding pitfalls and textbook errors

Ladislav Kavan[1]

Received: 9 November 2023 / Revised: 28 November 2023 / Accepted: 28 November 2023 / Published online: 4 January 2024
© The Author(s) 2024

Abstract
This paper reviews selected problems, which appear in literature dealing with TiO_2, SnO_2, and ZnO. Some of them have more universal impact to semiconductor electrochemistry. The electronic band structure is a key for understanding fundamental properties and for rational design of applications, but the uncertainty of specific values determined experimentally or by theoretical calculations should not be ignored. The inappropriate use of Mott-Schottky plot for characterization of certain semiconductor electrodes is another source of problems. Some other technical and formal issues in research and development of semiconductors are discussed.

Keywords Titanium dioxide · Tin dioxide · Zinc oxide · Mott-Schottky analysis; Photoelectrochemistry · Photocatalysis · Water splitting · Dye-sensitized and perovskite solar cells · Li-batteries

Introduction: *Errare humanum est*

Titanium dioxide, tin dioxide, and zinc oxide are among the generic materials, which triggered the success of semiconductor photo/electrochemistry in the mid of the twentieth century. Studies of these three n-type semiconductors revealed fundamental and practical incentives, which comprised, *inter alia*, development of photocatalysis, photovoltaics (dye-sensitized and perovskite solar cells), generation of solar fuels from abundant resources (water, N_2, or CO_2), and fabrication of Li-batteries. According to Web-of-Science, investigations of these three materials currently produce about 130 scientific documents per day! Such an information overload is also responsible for inconsistent data, oversimplifications, and conflicting interpretations.

Disclosing pitfalls in textbooks and scientific papers is an unrewarding job, like writing a negative referee's report or expelling a student from an exam. In all cases, the reviewer or examiner must convincingly articulate his/her arguments, as people usually do not protest positive evaluation, but do reject critical assessments. Yet, making errors in research and teaching/learning is very natural and omnipresent. (The trial/error is a strategy, not a disgrace.) The author of this article also made many mistakes in his research; some examples are listed at the end of this paper.

There are several good reviews on the properties and applications of oxide semiconductors. We can mention, e.g., the special issue of *Chem.Rev* [1] and the "coming-soon" book [2]. Consequently, there is no reason to write yet another text of this kind. My review is focused on open questions and problematic issues in the field, i.e., it is selective rather than comprehensive. I did my best to avoid subjective assortment of these topics, but it may happen that others are allergic to different glitches. In any case, my paper endeavors to highlight questionable issues and to aid students and teachers of electrochemistry.

Band structure and water splitting

Chemistry in general and electrochemistry in particular investigate the valence electrons in molecules (highest occupied molecular orbital, HOMO) and solids (valence band maximum, VBM). Photo(electro)chemistry pushes these electrons towards LUMO (lowest unoccupied molecular orbital) or CBM (conduction band minimum). Figure 1 shows the basic scheme of energy levels in n-doped semiconductors. Though it looks trivial, there are entries, which

✉ Ladislav Kavan
kavan@jh-inst.cas.cz

[1] J. Heyrovsky Institute of Physical Chemistry, Czech Academy of Sciences, Dolejskova 3, 18223 Prague 8, Czech Republic

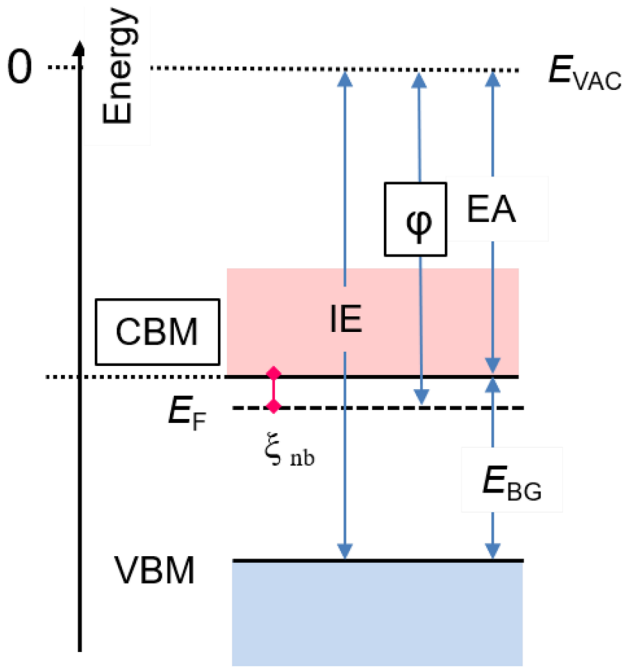

Fig. 1 Scheme of energy levels and the corresponding derived quantities for n-doped semiconductors. CBM and VBM are conduction band minimum and valence band maximum, respectively. The position of Fermi level is E_F. IE is the ionization energy, EA is electron affinity, φ is work function, and E_{BG} is the band gap. E_{VAC} is the reference energy of an electron at rest in vacuum

deserve attention. Due to n-doping, which is typical for TiO_2, SnO_2, and ZnO, the Fermi level (E_F) is upshifted towards the vicinity of CBM. Strictly speaking, the terms "Fermi energy" and "Fermi level" (electrochemical potential of electrons, μ_e) are not synonyms [3], but in the context of this article, we can omit subtle differences of both quantities. The offset of the Fermi level from energy of the conduction band minimum (E_{CBM}) is:

$$\zeta_{nb} = \frac{k_B T}{e} \ln\left(\frac{N_C}{N_D}\right) \quad (1)$$

k_B is the Boltzmann constant, T is temperature, e is electron charge, N_D is the concentration of donors, and N_C is the effective total concentration of conduction-band states at CBM:

$$N_C = 2\left(\frac{2\pi m^* k_B T}{h^2}\right)^{3/2} \quad (2)$$

h is the Planck constant, and m^* is the reduced mass of electron. (Eq. 1 is valid if all the donors are ionized, which is a reasonable assumption in most cases.) Table 1 lists the selected characteristics of TiO_2 (anatase, rutile), SnO_2, and ZnO, which are relevant to the follow-up discussion. The quoted numbers are just typical estimates from various values in literature.

Titanium dioxide has four naturally occurring phases: tetragonal rutile and anatase, orthorhombic brookite, and a quite rare monoclinic TiO_2(B). Furthermore, there are at least seven additional synthetic polymorphs of TiO_2. Rutile is reported to be the thermodynamically stable form of TiO_2. However, if the crystal dimensions drop below ca. 10–20 nm, anatase becomes the stable polymorph of

Table 1 Selected characteristics of TiO_2 (anatase, rutile), SnO_2, and ZnO. The average values of V_{fb} were determined from the Gaussian fits of histograms of the flatband potential distribution compiled from literature (see Fig. 4 and ref. [16] for details)

	TiO_2 anatase	**TiO_2 rutile**	**SnO_2 cassiterite**	**ZnO wurtzite**
Crystallographic space group	$I4_1/amd$	$P4_2/mnm$	$P4_2/mnm$	$P6_3mc$
Dielectric constant, ε_r	55	173	10	7.9
Band gap, E_{BG} eV (optical transfer type)[a]	3.2 (i)	3.0 (qd)	3.6 (d)	3.3 (d)
Effective density of states @ CBM, N_C [cm^{-3}]	$8{\cdot}10^{20}$	10^{20}–10^{21}	$4{\cdot}10^{18}$	$2{\cdot}10^{18}$
Point of zero charge, pH_{PZC}	5.4	5.9	3–5; 8.2[b]	8–9.5
Reduced mass of electron, (m^*/m_0)[c]	10	3–30	0.3	0.215
Limiting thickness of depl. layer, W_{lim} [nm][d]	3	4–14	17	21
Average flatband potential, V_{fb} [V vs. RHE][e]	0.163	0.050	0.342	0.223
Average V_{fb} for single crystals only [V vs. RHE][e, f]	−0.133	0.049	≈0.4 ?[f]	0.233
Change of V_{fb} with pH [mV/pH][e,g]	−60 ± 6	−60 ± 6	−50 ± 27	−43 ± 16[g]

[a]Indirect (i), direct (d), quasi-direct (qd)

[b]Specifically for ALD-SnO_2 [23]

[c]The entry m_0 is the mass of electron at rest ($9.109{\cdot}10^{-31}$ kg)

[d]Assuming $N_D = N_C$ ($\zeta_{nb} = 0$) and 1 eV band bending

[e]From all the published studies compiled in [16] (505 values for TiO_2, 97 values for SnO_2, and 223 values for ZnO in total)

[f]Not enough data for statistical analysis of SnO_2 (cassiterite). The published values (in V vs. RHE) are 0.31, 0.44 and 0.56 [16], but the last entry is, probably, an error [23, 25]

[g]The specific value for ZnO thin films is (−4.8 ± 2.3) mV/pH. The value for all morphologies, excluding thin films, is (−67 ± 21) mV/pH. (The expected Nernstian shift is -59 mV/pH) [16]

TiO_2. This is reminiscent of the allotropic forms of carbon, where thermodynamic stability of diamond/graphite, reportedly flips too in the nano-world [4].

Figure 2 shows the calculated positions of CBM/VBM for eight common titania polymorphs related to the position of the redox potentials of H^+/H_2 and O_2/H_2O [5]. A prototype diagram of this kind (quoting experimental data for TiO_2, SnO_2, ZnO, GaAs, GaP, CdSe, CdS, and SiC) was presented in 1975 by Gleria and Memming [6]. The motivation for comparing the band edges with electrochemical potentials of water is obvious: if these redox potentials are located at positions, which are inside the band gap, the direct photoelectrolysis of water is possible without external bias. More specifically, the bias-free photoelectrolysis of water requires that the conduction band minimum (CBM) is higher than the energy corresponding to the H^+/H_2 redox potential, and the valence band maximum (VBM) is lower than that of the O_2/H_2O redox potential.

The discovery of "bias-free" electrolysis of water at a photoexcited rutile single crystal anode and Pt-cathode is habitually credited to Fujishima and Honda [7], despite Boddy [8] published a very similar work four years before this seminal paper appeared. (In fact, 5 years, if we count the Dallas Meeting of the Electrochemical Society in 1967.) Another problem of this famous work is the suspected omission of "chemical bias" originating from the pH-gradient in the cell. In fact, rutile appears to have too low CBM to split water effectively (cf. Fig. 2 and ref. [9] for detailed discussion).

Diagrams showing CBM/VBM of common semiconductors appear in almost every textbook or review article dealing with semiconductor electrochemistry, and in many special papers, too. It should be noted that authors often omit citation to where the band energies come from. (The pioneering paper [6] is a rare exception to this rule.) Though being so popular, these diagrams are also sources of numerous problems.

The first issue is the energy scale: physicists use the energy of electron at rest in vacuum (E_{VAC}) as their reference zero (Figs. 1 and 2, left axis). Electrochemists use the standard hydrogen electrode (SHE) as their reference zero (Fig. 2, right axis). These two scales are difficult to interrelate, even if we forget that *energy* and *potential* are different physical quantities. Furthermore, the relation of both scales requires adopting the concept of "absolute electrode potential," which, for fundamental reasons, cannot be expressed accurately. A practical way-out is the IUPAC recommendation by Trasatti [10], to use the value of -4.44 ± 0.02 eV for the absolute potential of SHE at 298.15 K. However, others quote different numbers, e.g., -4.5 eV [3]. Eventually, students are confused by the fact that a *downshift* of an energy level in the physical scale means an *upshift* in the electrochemical scale (cf. the arrows in Fig. 2).

Another formal flaw is that some authors (including the pioneers [6]) used the normal hydrogen electrode (NHE), instead of SHE for indexing their band diagrams. Though the difference between SHE and NHE is small (≈5.7 mV), we should avoid NHE because it is not a recognized electrochemical standard [11]. Particularly in the discussion of water splitting, a practical reference system is the so-called reversible hydrogen electrode (RHE). The potential of RHE is:

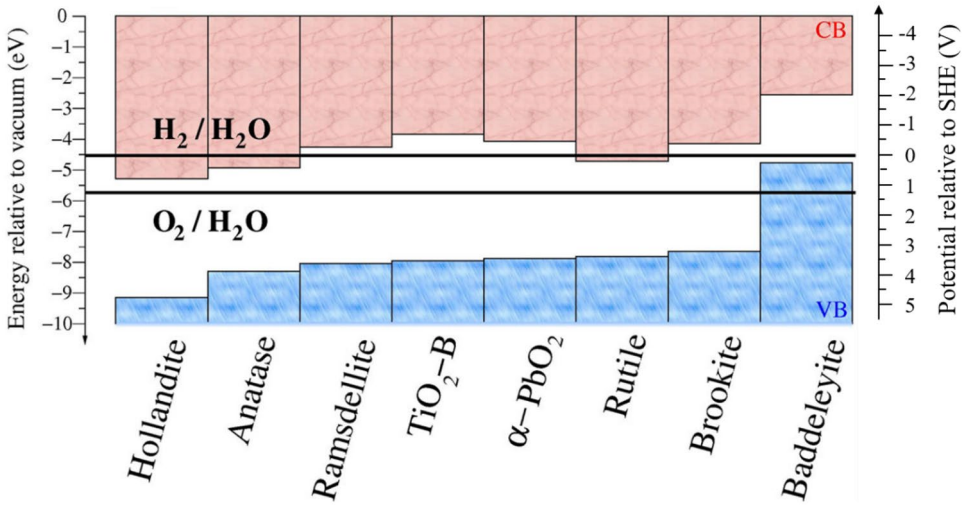

Fig. 2 Positions of conduction band (CB) and valence band (VB) calculated by density functional theory (DFT) for eight different TiO_2 polymorphs. (The α-PbO_2 (columbite)-type phase of titania is sometimes labeled TiO_2(II) or α-TiO_2.) The positions are referenced to the e-vacuum scale (left axis) and to the scale of standard electrochemical potentials (vs. SHE; right axis). The band positions are compared with the levels corresponding to redox potentials of H^+/H_2 and O_2/H_2O in aqueous medium at pH≈0. Adapted with permission from [16]. Copyright (2015) American Chemical Society

$$V_{\mathrm{RHE}} = V_0 + \frac{RT}{F}\ln\frac{a_{\mathrm{H^+}}}{(p_{\mathrm{H2}}/p_0)^{1/2}} \cong -0.059 \cdot \mathrm{pH} \quad [\mathrm{V}] \qquad (3)$$

V_0 is the standard potential of $H^+(aq)/H_2(g)$ redox couple (defined as 0.000 V at all temperatures), R is the gas constant, F is Faraday constant, a_{H+} is the activity of $H^+(aq)$, p_{H2} is the fugacity of $H_2(g)$, and p_0 is the standard pressure (1 bar). For a detailed discussion of SHE and RHE see [12]. The RHE scale is useful, e.g., for presenting the flatband potential, V_{fb} which is equivalent to the Fermi level position at zero band bending ($E_{F,fb}$):

$$E_{\mathrm{F,fb}} = -\varphi_{\mathrm{fb}} = eV_0^{\mathrm{SHE}} - eV_{\mathrm{fb}} = E_{\mathrm{CBM}} - \xi_{\mathrm{nb}} \qquad (4)$$

V_0^{SHE} is the potential of SHE in the absolute scale; $V_0^{\mathrm{SHE}} \approx -4.44$ V [13]. The entry φ_{fb} is the work function derived from the flatband potential (also called "electrochemical work function") [14]. There is a common mistake in the literature that electrode potentials on the RHE scale are recalculated to the absolute scale using the −4.44 V value. This is valid only if the experiment was carried out at pH 0; at another pH, one must properly recalculate from RHE to SHE (Eq. 3). The second problem associated with Eqs. 3 and 4 is that the electrochemical work function, φ_{fb} should be correctly calculated for pH corresponding to the point of zero-charge of the given semiconductor (Table 1) [15]. This is a non-trivial task, because the $V_{fb} = V_{fb}(\mathrm{pH})$ function is complicated and material-specific (see below and Table 1).

Considering Eq. (3), one could argue that positioning the energy level of H^+/H_2 above CBM could be simply carried out by decreasing the pH. However, the idea of "pH engineering" is a bit problematic. The band edges (CBM/VBM) are reported to move with pH in the same way, due to the acidobasic equilibria (protonation/hydroxylation) at the oxide semiconductor surfaces.

The assumption of parallel Nernstian shifts of CBM/VBM and hydrogen (oxygen) redox potentials may or may not be true. Patel et al. [16] showed that there are semiconductor electrodes, such as ZnO thin films, whose CBMs/VBMs are virtually pH-independent. (This work actually analyzed flatband potentials, not CBMs, but both quantities differ just by a constant, ζ_{nb}.) The physical reason for this anomaly has not yet been clearly elucidated; one hypothesis is based on the finding that the abundant crystal face (0001) on ZnO (wurtzite) can be capped either by O atoms or Zn-atoms, and this induces a varying surface polarity [16].

Yet another fundamental problem of the energy diagrams (Figs. 1 and 2) is that the CBM, VBM, and work functions are trivially regarded as material constants, independent of experimental or theoretical techniques used for their determination. However, this is not true. A standard technique to measure work function and VBM is the ultraviolet photoelectron spectroscopy (UPS) and X-ray photoelectron spectroscopy (XPS) in ultrahigh vacuum. Actual experimental values, e.g., for the work function of the TiO_2 anatase (001) surface, fluctuated between 3.61 and 6.76 eV depending on details of sample cleaning and pretreatment [17]. The chaos is further boosted in polycrystalline samples. For instance, Zhu et al. [18] positioned the CBM of polycrystalline rutile slightly below that of anatase, contradicting most UPS/XPS works of others [19–21].

Mansfeldova et al. [15] revisited the problem by using several experimental methods for testing of four different TiO_2 surfaces, viz. anatase (101), anatase (001), rutile (001), and brookite (100). Figure 3 shows example data for anatase and rutile. In accord with the "mainstream" literature, rutile had smaller work function than anatase from UPS. This finding was reproduced by the near-ambient-pressure (NAP) UPS in the presence of 0.5 mbar of H_2O (g), by Kelvin probe measurements in ambient air, and by the flatband potentials in acetonitrile electrolyte solution. But in contrast to aprotic medium, the φ_{fb} of rutile was larger than that of anatase in an aqueous electrolyte solution (Fig. 3).

Deak et al. [22] proposed that flipping of the band alignment of anatase/rutile in aqueous electrolyte solution is caused by dissociative adsorption of water (cf. right part of Fig. 3). The histogram of work functions is updated for SnO_2 (cassiterite) (001) and for ZnO (wurtzite) from other works [14, 23–25]. Specifically, for ZnO, we can distinguish slightly different values for the O-terminated and Zn-terminated (0001) faces [14].

The crucial information is that the work functions and the corresponding CBMs fluctuate over a range of more than 1 eV, even on the well-defined single crystal surfaces, depending on experimental techniques and the actual sample environment. This makes an appeal for cautious discussion of these energy levels in textbooks and special papers. Also, care should be taken when using, e.g., tabled data from various handbooks. The only quantity, which is robust enough (i.e., the "true" material constant), is the band-gap, E_{BG} (Table 1). It is conveniently measured by a Tauc plot or by an electrochemical Tauc plot (for details, see [26]).

Determination of flatband potential and donor concentration by Mott-Schottky analysis

The flatband potential, V_{fb} can be determined by various spectro/photo/electrochemical techniques [16, 27], but the so-called Mott-Schottky analysis is surely the most popular one. It is based on the measurement of potential-dependent capacitance (C) at a semiconductor/electrolyte solution interface. In one single experiment, we get two useful parameters: the flatband potential and the

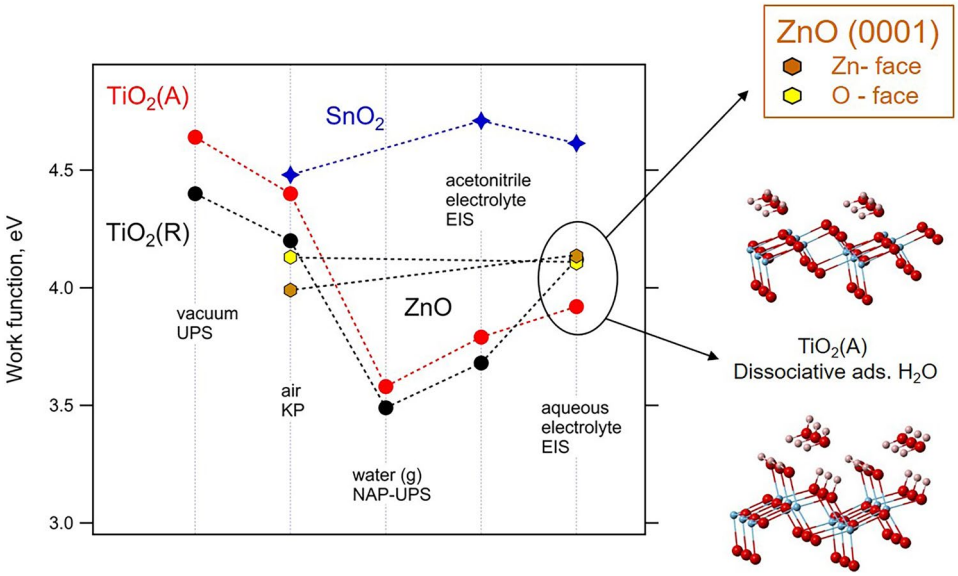

Fig. 3 The experimental work functions for single crystal surfaces determined by ultraviolet photoelectron spectroscopy (UPS), Kelvin probe (KP), near-ambient pressure UPS (NAP-UPS), and by Mott-Schottky plots from electrochemical impedance spectra (EIS) measured in acetonitrile or aqueous electrolyte solutions. TiO_2(A) is anatase (101) face (red points); TiO_2(R) is rutile (001) face (black points). Data reprinted with permission from [15]. Copyright (2021) American Chemical Society. The previously published plot is here updated by new data for SnO_2 (cassiterite) (001) (blue stars) [23, 25] and for ZnO (wurtzite) [14, 24]. Brown hexagons are for the Zn-terminated (0001) face and yellow hexagons for the O-terminated ($000\bar{1}$) face

concentration of majority charge carriers, i.e., donors in the case of n-type semiconductors, N_D. The Mott-Schottky equation for this interface reads:

$$\frac{1}{C^2} = \left(\frac{2}{e\varepsilon_0\varepsilon_r N_D}\right)\left(V_{app} - V_{fb} - \frac{k_B T}{e}\right) + \frac{1}{C_H^2} \quad (5)$$

ε_0 is the permittivity of free space, ε_r is the dielectric constant (Table 1), and V_{app} is the applied potential. The Helmholtz capacitance, C_H, is assumed to be of the order of tens of μF/cm^2. It is often supposed to be much larger than the space-charge capacitance, thus causing negligible contribution to Eq. 5. This may or may not be true.

The overall capacitance, C, is determined by electrochemical impedance spectroscopy (EIS). The simplest variant, which is embedded in software of some potentiostats with frequency–response analyzers, is the calculation of C at a fixed circular frequency, ω. Other frequencies will give, almost always, different C values, and this leads to a conceptually problematic finding of *frequency dispersion* of Mott-Schottky plots [28]. The dispersion is sometimes discussed in terms of "structural perfection" of the semiconductor, but this perception is questionable, too. One could ask: why the V_{fb} and N_D values of good samples should be frequency-dependent?

A straightforward way out is the fitting of the complete impedance spectrum, determined at all used frequencies, to certain Randles-type equivalent circuit. The constant phase element (CPE) is usually preferred over a simple capacitor particularly for polycrystalline thin films (for an overview of equivalent circuits see [29, 30]; for a general discussion of CPE, see [31]). The impedance of CPE equals [15, 23, 31]:

$$Z_{CPE} = B^{-1}(i\omega)^{-\beta} \quad (6)$$

B (admittance pre-factor) and β are the frequency-independent parameters of the CPE. The interfacial capacitance, C is then calculated from:

$$C = \frac{(R_{CT} \cdot B)^{1/\beta}}{R_{CT}} \quad (7)$$

R_{CT} is the charge-transfer resistance, which is deconvoluted from the EIS fitting, too. The measurement must be carried out on well-defined surfaces, ideally on single crystal electrodes. (In this case, the use of CPE (Eqs. 6 and 7) seems to be overestimated, but CPE converts to a pure capacitor for $\beta = 1$.) Polycrystalline electrodes (e.g., thin films on substrates) are also acceptable, provided they are free from pinholes. This can be simply checked by voltammetric blocking tests [23, 32–35]. On the other hand, porous electrodes, such as nanospheres [36] nanorods [36, 37] or nanotubes [16] are, in general, too complicated (if not inapplicable) for the Mott-Schottky analysis. Theoretical treatment was pioneered by Bisquert et al. [36] and Peter et al. [37]; general discussions were presented by Sivula [38] and Hankin et al. [30]. In certain cases (e.g., in amorphous thin films), the single-frequency impedance could still provide

useful information [39], but the deconvolution of a complete EIS-spectrum is generally preferable for high-quality crystalline thin films and single crystal electrodes [30].

Strictly speaking, the assumption about the overall perfection of single crystal electrodes is unfaithful, too. For instance, the TiO_2 (anatase) single crystal is usually purchased, while manufacturers cut it from natural minerals. These, of course, contain impurities, such as Fe. Iron tends to segregate upon thermal treatment, up to even overgrowth of iron oxide on the TiO_2 surface [40]. The laboratory growth of sufficiently large anatase single crystal is uneasy and time-consuming [41]. Furthermore, the synthesis requires an addition of structure-directing impurities (Al, Nb) in concentrations ≈0.2% [40, 41]. Eventually, the crystal is not "atomically flat," but can contain terraces [42].

Patel et al. [16] compiled flatband potentials in aqueous media (505 values for TiO_2, 97 values for SnO_2, and 223 values for ZnO). A striking output from their analysis is the huge spread in the literature data (Fig. 4). For instance, the flatband potentials for TiO_2 varied over a range as large as > 1.5 V (Fig. 4b), clearly documenting that some values are false. Indeed, the distribution for TiO_2 is narrowed by eliminating data for anatase nanotubes, which are principally unsuitable for these studies (see above and Fig. 4d). The width of the depletion layer (W) on a flat n-type semiconductor surface equals:

$$W = \left(\frac{2\epsilon_0\epsilon_r}{eN_D}\right)^{1/2}\left(V_{app} - V_{fb} - \frac{k_B T}{e}\right)^{1/2} \quad (8)$$

Table 1 compiles the limiting values (W_{lim}) calculated for $N_D = N_C$ and for the applied potential of 1 V referenced to V_{fb} (the band bending). The calculated values for TiO_2, SnO_2, and ZnO are from 3 to 21 nm (Table 1). This is the minimum film thickness to fully accommodate the space charge layer, thus allowing for an unperturbed measurement of EIS. Yet, the penetration of the depletion layer into the substrate can sometimes be traced on good-quality films [34].

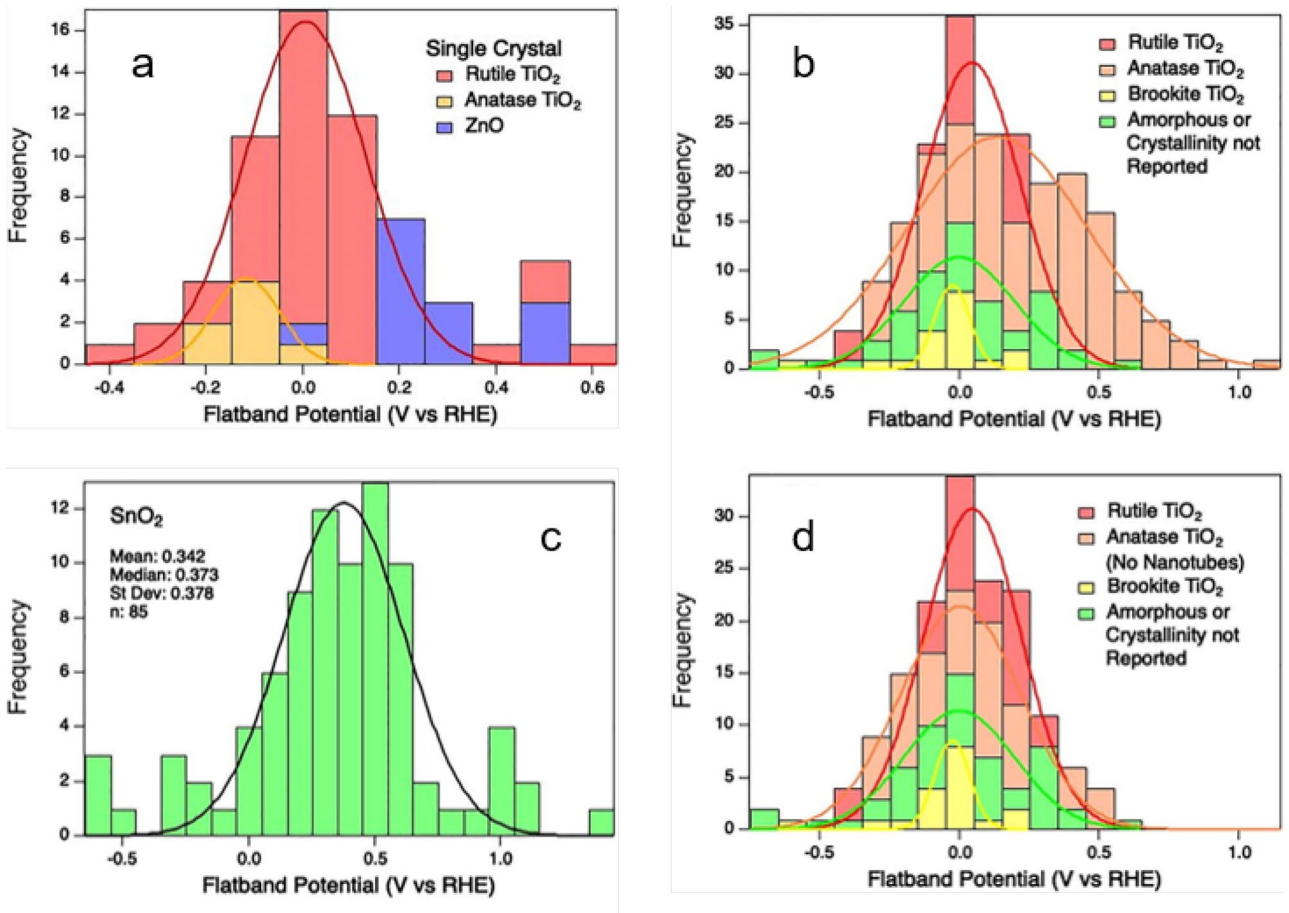

Fig. 4 Histograms of the flatband potential distribution and the corresponding Gaussian fits (if relevant) for **a** single crystals TiO_2 (anatase, rutile) and ZnO (wurtzite), **b** different phases of TiO_2 in all morphologies, **c** all forms of SnO_2, and **d** TiO_2 as in chart (b), but without anatase nanotube data points. Reprinted with permission from [16]. Copyright (2022) AIP Publishing

The space-charge layer thickness is conceptually related to the Debye length (L_D) which is a distance over which the charge carriers screen the local electrical field:

$$L_D = \left(\frac{\varepsilon_0 \varepsilon_r k_B T}{e^2 N_D} \right)^{1/2} \quad (9)$$

For low-doped spherical nanoparticles, the Debye length, L_D, is much larger than the particle radius, i.e., the band-bending is unlikely. This is further complicated in mesoporous thin films, used, e.g., in dye-sensitized (Grätzel) solar cells [43, 44], in which nanoparticles interconnect and the electrolyte solution resides in mesopores. Bisquert et al. [36] provided rationale for negligible band bending in this case. Hence, the mesoporous film is yet another system, in which the Mott-Schottky analysis fails for principal reasons [45].

Incorrect flatband potentials are not the only issue of the Mott-Schottky plots. The analysis of otherwise good samples (e.g., non-porous thin films) tends to overestimate the donor densities as compared, e.g., to Hall-effect measurements [32]. More specifically, the N_C calculated from Eq. 2 (Table 1) gives the upper estimate of N_D assuming the semiconductor is still non-degenerated. The limiting value means that the Fermi level coincides with CBM ($\zeta_{nb} = 0$).

Values of N_D exceeding N_C would indicate a degenerated semiconductor, which is hardly the case in most studies. For instance, SnO_2 thin films do not show any metal-like electrochemistry (like, e.g., the F-doped SnO_2, FTO), but instead—a perfectly rectifying behavior [23, 32, 33]). This contradiction is implicitly present in many literature values of N_D [16, 38]. Another point to highlight is that the flatband potential provides the position of the Fermi level (Eq. 2) *not* the conduction band edge. This mistake appears frequently in the literature (for collection of papers infected by this error, see [16]).

Calculation of work functions and band edges by DFT

Most DFT (density function theory) calculations are made for perfect single crystals surrounded by vacuum, which is usually not articulated in the specific works. Calculations of two interacting phases [20, 46], non-stoichiometric surfaces [47], small nanocrystals [48], or crystals interacting with, e.g., water [22] are less often encountered in the literature. (Strictly speaking, the oxide semiconductors used in electrochemistry are hardly stoichiometric at all; the n-doping is often attributed to a small oxygen deficiency, e.g., TiO_{2-x}; $x \approx 0.01$.) Theoretical modelling by Zhang and Dong [20] revealed that the interface itself can reverse the CBM alignment of the coupled and isolated TiO_2 phases. Analogously, Ko et al. [48] predicted that the CBM alignment of anatase/rutile will flip for nanocrystals below ≈15 nm in size.

Calculations for "ideal" conditions and bulk crystals systematically put the CBM of TiO_2 (anatase) slightly below that of rutile (as in Fig. 2). This prediction is confirmed by a majority of UPS/XPS experiments, which are usually, but not necessarily always, made in ultrahigh vacuum [15, 17, 21]. Resolving the controversy about band alignment between anatase and rutile TiO_2 would require computational modelling of more realistic systems, ideally a semiconductor surface contacting an electrolyte solution. Unfortunately, treatment of this electrochemical interface is beyond the capabilities of the current super-computers.

A drastic simplification of the Helmholtz layer by just two monolayers of water molecules provides a model, which can be reasonably treated by DFT calculations. Interestingly, the flipping of CBM positions in TiO_2 anatase/rutile is confirmed even by this primitive model. More specifically, the electrochemical interface composed of an anatase (101) surface covered by one monolayer of dissociated water and one monolayer of molecular water above it (cf. Fig. 3) provides a plausible computational background for the CBMs flipping [22].

Photoelectrochemistry: beyond the Gärtner-Butler model

Theory of electron transfer at the semiconductor/electrolyte solution interface was developed in 1959–1966 by W.W. Gärtner and H. Gerischer, and later updated by M. A. Butler. It has been very useful and didactically rewarding, as it elegantly explained photoelectrochemical reactions occurring on semiconductor electrodes, illuminated by photons with energies larger than E_{BG}. The model elucidates why and how the faradaic processes are driven by the electron/hole separation (exciton dissociation) in the built-in electrical field of the space-charge layer and the subsequent drifting of photoholes to the interface (Fig. 5a).

More precisely, in addition to the holes generated inside the space charge region, the classical model also considered holes in the close vicinity of the depletion layer. These holes can still reach the interface by diffusion, and contribute to the photocurrent at a probability $P(x)$:

$$P(x) = e^{-x/L_p} \quad (10)$$

x is distance from the interface, and L_p is the hole diffusion length. Within this approximation, the photocurrent on thin-film electrodes does not saturate, when the film thicknesses exceed the depletion layer width, W (see Eq. 8), but at the thicknesses exceeding the photon-attenuation depth.

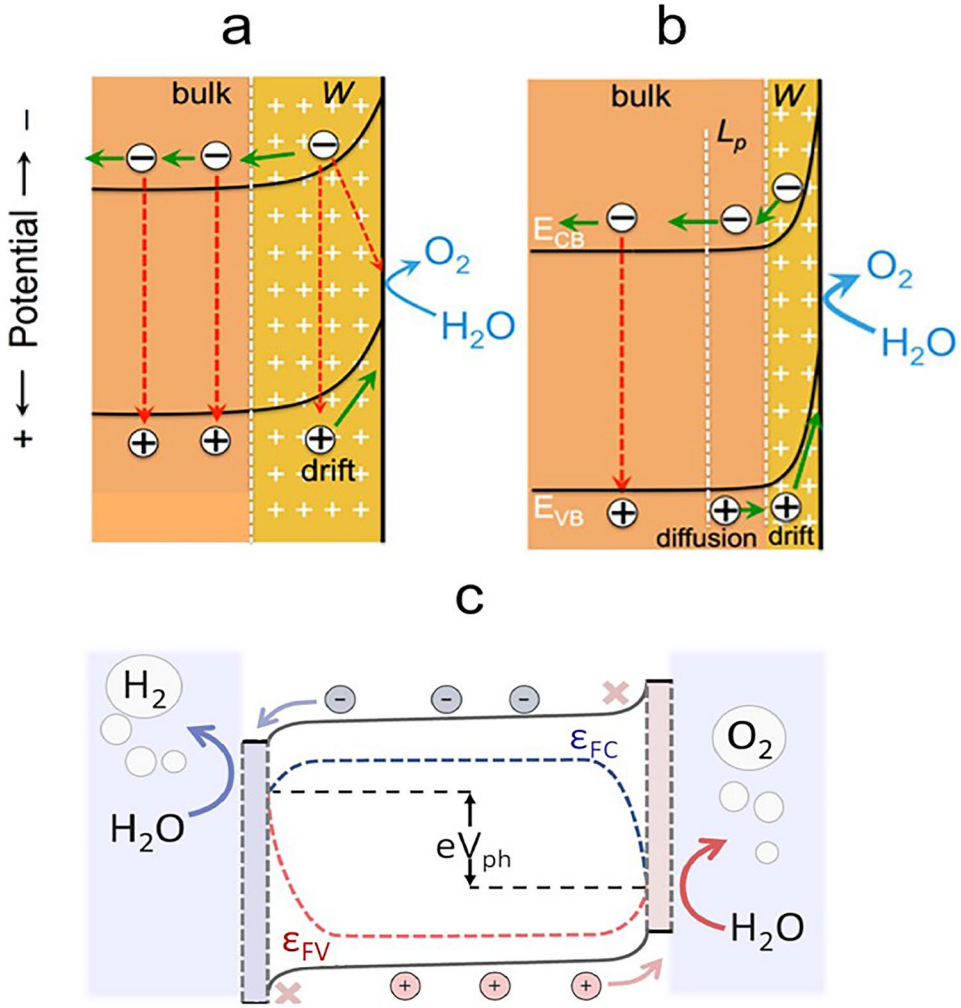

Fig. 5 Band bending and charge carrier dynamics at the photoexcited semiconductor contacting electrolyte solution. Red dashed arrows indicate recombination. **a** The exciton dissociation occurs exclusively in the built-in electrical field of the depletion layer (thickness *W*). **b** The exciton dissociation occurs also outside the depletion layer. Some photogenerated holes are transported towards the interface by diffusion. L_p is the hole diffusion length. Reprinted with permission from [93] Copyright (2016) American Chemical Society. **c** Scheme of a photoelectrochemical cell under illumination. The quasi-Fermi levels of electrons and holes are annotated as ε_{FC} and ε_{FV}, respectively. They merge and align with the respective Fermi levels of the metallic contacts at both terminals of the cell. V_{ph} is the photovoltage. Reprinted with permission from [51]. Copyright (2022) the Royal Society of Chemistry

It is defined as a thickness, at which the optical density of 1 (i.e., 90% light absorption) is achieved for incident photons [49]. This *diffusion-drift model* is schematized in Fig. 5b.

In the last decade, additional studies have shown that the diffusion-drift model was still not sufficient for description of some systems. For instance, ZnO thin-film electrodes exhibited photocurrents, which did not saturate for film thicknesses equal to the photon attenuation depth, but increased further in thicker films [49]. The deviation was attributed to the long-range backward diffusion of excitons. This effect is important for semiconductors with large exciton binding energies (such as ZnO; ≈60 meV), but small for semiconductors with weakly bond excitons (e.g., TiO_2 and Fe_2O_3) [49]. (Note, however, a conflicting work about TiO_2 anatase single crystal and nanoparticles [50]).

Recently, Schleuning et al. [51] presented yet another concept to account for deviations from the Gärtner-Butler model. Figure 5c shows a scheme of the full photoelectrochemical cell for water splitting. This model highlights the role of electron- or hole-selective contacts, which actually control the photovoltage, V_{ph}. In other words, the gradient of quasi-Fermi levels of electrons and holes is the fundamental driving force for these photoelectrochemical reactions. Moreover, many devices operate without any significant built-in electric fields (e.g., dye-sensitized solar cells; see below).

Applications: photocatalysis and superhydrophilicity

Titania is the key material for photocatalysis, and it has been intensively debated how the band structure influences its activity. In general, rutile is regarded better reductant, and anatase is a better oxidant in photocatalytic reactions [52]. This resonates with the smaller work function of rutile, which is observed in majority of experiments and calculations (see Figs. 2 and 3 and discussion thereof). The

photocatalytic applications often favor mixed-phase TiO_2 (anatase/rutile) composites, from which the P25 (Degussa/Evonik) is surely the most popular benchmark material. A systematic study by Yaemsunthorn et al. [52] confirmed that the anatase/rutile composites exhibit synergistic effects in photocatalysis, as compared to pure phases.

The simplest explanation of this synergy follows from the band alignment at the interface (Fig. 6) [53]. It provides additional driving force for exciton dissociation, in which the photoexcited electrons are pushed towards the CBM of anatase and photoholes towards the VBM of rutile. Nevertheless, other factors need to be considered, too. They comprise efficiency of charge separation, lifetime of photogenerated charges, light absorption, redox characteristics, porosity, surface area, and the specific reaction/s, for which the photocatalyst is optimized [52].

The second issue, which is often ignored, is the flipping of flatband potentials (CBM positions) at the aqueous electrochemical interfaces [15]. A rare exception to this rule is the work of Nosaka and Nosaka [53]. They proposed that the V_{fb} for anatase, measured by Mott-Schottky plot, is related to the minimum *direct* band gap of ≈3.8 eV (Fig. 6). The direct CBM is hit, if the EIS-measurement sweeps potentials from lower to higher values. This explanation would elegantly address the contractions, even quantitatively: Fig. 6 confirms that the direct CBM of anatase is by 0.2 eV above the CBM of rutile. Nevertheless, this idea still requires experimental verification, whether or not the scan direction is really that important. Another objection is that the reference studies were made on high-quality single crystals, but photocatalysts are usually imperfect materials, up to suspended nanoparticles, which are outside any electrochemical control. Small nanoparticles and interacting phases can exhibit different anatase/rutile alignment, too [20, 46, 48].

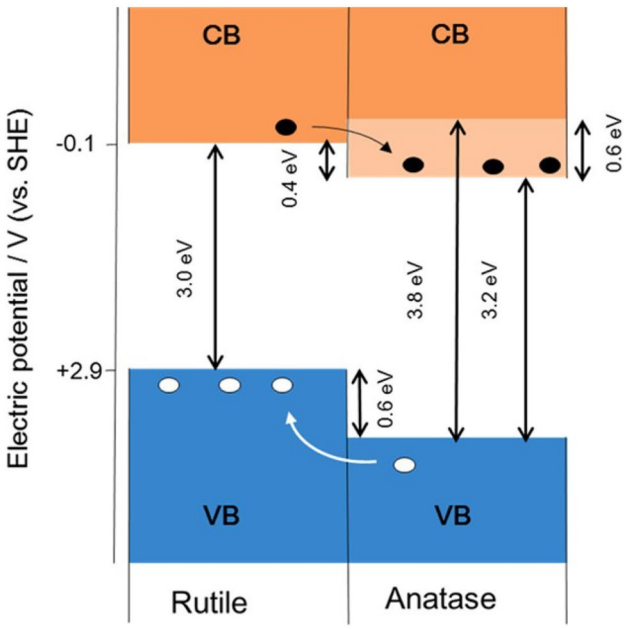

Fig. 6 Proposed band alignment for the rutile and anatase forms of TiO_2 considering the direct (3.8 eV) and indirect (3.2 eV) band gaps for anatase. Data reprinted with permission from [53]. Copyright (2016) American Chemical Society

The synergic effect, which improves the photocatalytic activity of TiO_2, can be, however, detrimental in other applications, such as in cosmetics and cotton textiles [54]. For instance, larger toxicity of mixed-phase TiO_2 manifests itself by enhanced injury of human skin during sunlight exposure, which is proven by both in vitro and in vivo experiments [54].

The photoinduced wettability of the TiO_2 surface ("superhydrophilicity") is another issue in photocatalysis. Since its discovery in 1997, it generated significant experimental and theoretical efforts, aiming at explanation of this spectacular effect. It manifests itself as perfect spreading of water droplets over photo-treated titania, which attain, eventually, a contact angle close to 0° [55]. Various practical applications of the TiO_2-coated glass, e.g., for antifogging windows and mirrors, are at hand.

The effect was attributed to structural changes of the TiO_2/H_2O interface, re-arrangement of hydrogen bonds, H_2O-clusters etc. XPS and IR-spectroscopy supported a partial photocatalytic removal of hydrocarbon impurities, too [55]. Nevertheless, a subsequent work by Diebold et al. [56] elegantly clarified, that the UV-induced superhydrophilicity in ambient environment is actually caused by selective adsorption/photodegradation of airborne carboxylic acids, rather than by structural modifications of the TiO_2 surface. This approach elucidated also the reverse dark reaction, which is hard to understand in terms of the water rearrangement on the surface.

Applications: dye-sensitized (Grätzel) solar cell

The discovery of a dye-sensitized solar cell (DSSC) [57], also called the Grätzel cell, triggered significant scientific and industrial efforts during the last three decades [43, 58]. The record efficiency of DSSCs is currently 15.2% [58]. All the discussed oxide semiconductors (TiO_2, SnO_2, ZnO) are useful as the photoanode materials, but the nanocrystalline TiO_2 (anatase) in mesoporous thin film clearly dominates. The photoanode is sensitized to visible light by a suitable dye, which is interfaced to an electrolyte redox mediator. The latter serves for reductive regeneration of the dye, which becomes oxidized after electron injection from LUMO into the CBM of TiO_2 (Fig. 7). The open circuit photovoltage (V_{OC}) of the solar cell under sunlight equals:

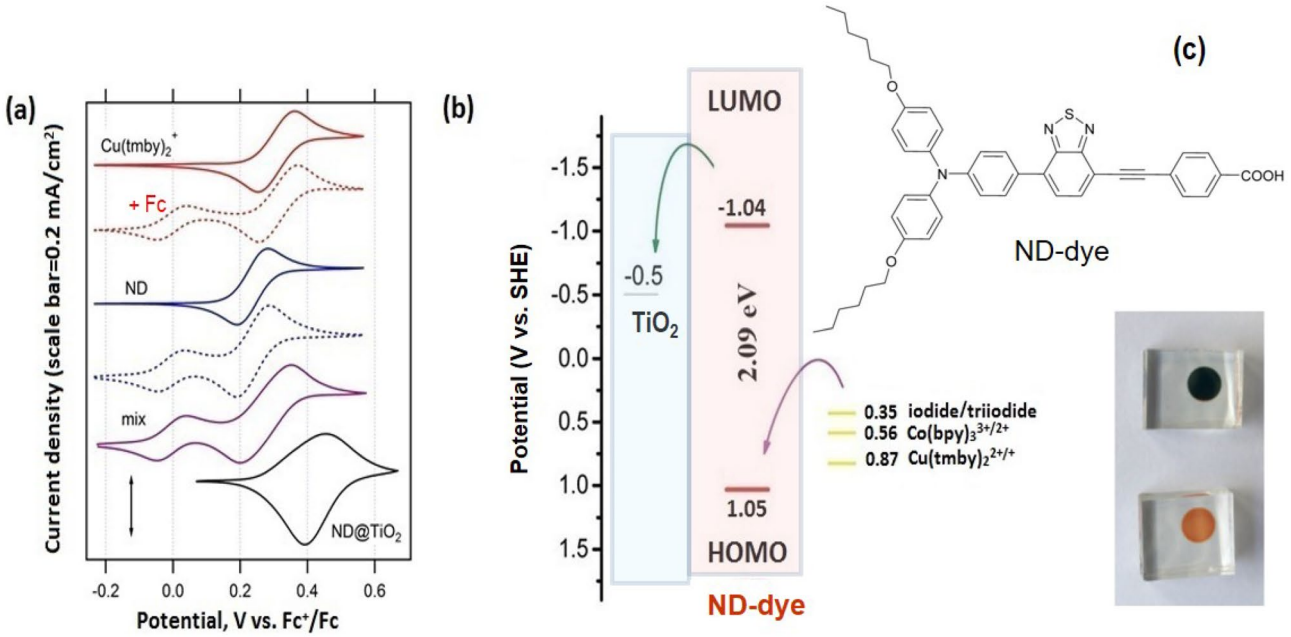

Fig. 7 **a** Cyclic voltammograms in dichloromethane electrolyte solution; from top to bottom: $Cu(tmby)_2^+$, *ditto* upon addition of ferrocene (Fc, red dashed), ND-dye (blue), *ditto* upon addition of ferrocene (blue dashed), mixture of ND + $Cu(tmby)_2^+$ + Fc (magenta). The last voltammogram (black) is for the ND-dye adsorbed on the TiO_2/FTO electrode. For recalculation, the Fc^+/Fc potential was set to 0.624 V vs. SHE. **b** Schematic diagram of the energy levels of TiO_2, ND-dye, and three typical redox mediators. **c** The formula of ND-dye and photograph of ND@TiO_2/FTO electrodes with the dye in in the ground state (orange, bottom) and after the electrochemical oxidation (black, top). Adapted with permission from [62]. Copyright (2018) John Wiley and Sons

$$V_{OC} = \frac{E_{CBM}}{e} + \frac{kT}{e}\ln\left(\frac{n_{ph}}{N_C}\right) - M_{redox} \tag{11}$$

n_{ph} is the number of photogenerated electrons in a semiconductor, and M_{redox} is the standard redox potential of the mediator. The open-circuit photovoltage is then determined from the difference between the maximum achievable quasi-Fermi level of electrons in the semiconductor film (the sum of the first two terms in Eq. 11) and the redox potential of the mediator (the third term in Eq. 11). Typical mediators are:

$$I_3^- + 2e^- \rightarrow 3I^- \; M_{redox} = 0.35\ \text{V} \tag{12a}$$

$$[Co(bpy)_3]^{3+} + e^- \rightarrow [Co(bpy)_3]^{2+} \; M_{redox} = 0.56\ \text{V} \tag{12b}$$

$$Cu(tmby)_2^{2+} + e^- \rightarrow Cu(tmby)_2^{+} \; M_{redox} = 0.87\ \text{V} \tag{12c}$$

$$Cu(dmby)_2^{2+} + e^- \rightarrow Cu(dmby)_2^{+} \; M_{redox} = 0.97\ \text{V} \tag{12d}$$

bpy is the 2,2′-bipyridine, tmby is the 4.4′,6,6'-tetramethyl-2,2′-bipyridine, and dmby is the 6,6′-dimethyl-2,2′-bipyridine. Mediators beyond I_3^-/I^- were developed in parallel with novel donor-π-acceptor dyes (such as ND in Fig. 7). This allows enhancement of V_{OC} of the solar cell (Eq. 11 and Fig. 7). The M_{redox} is theoretically limited only by the redox potential of the dye's ground state (≈1 V vs. SHE). Interestingly, the driving force for dye regeneration can be as small as ≈0.1–0.2 V in certain $Cu^{2+/+}$-mediated DSSCs (cf. Figure 7 and [58, 59]).

The second possible strategy for boosting V_{OC} is the upshift of the quasi-Fermi level of the semiconductor photoanode. It can be achieved by electrolyte additives [60] or by engineering of the semiconductor's CBM [61]. Unfortunately, most additives have detrimental effect on the ionic diffusion and charge-transfer rate at the counter-electrode, specifically for the $Cu^{2+/+}$-mediators, and this problem is yet to be solved [60]. The other issue is the ubiquitous uncertainty in the position of Fermi level of the semiconductor (cf. Figure 3). The value in Fig. 7 is just a guess (−0.5 V vs. SHE in the electrochemical scale, translating into the work function of ≈3.9 eV [62–64]). The experimental φ_{fb} for single crystal anatase (101) face is about 3.8 eV (for acetonitrile electrolyte solution; Fig. 3), but a more authentic measurement at polycrystalline thin film anatase in the DSSC-electrolyte solutions yielded values from 4.16 to 4.27 eV [33].

Figure 7 also demonstrates the frequent error of using the redox potentials of dyes in solution instead of the redox potentials of dyes adsorbed on the TiO_2 photoanode. The difference could even generate a curious conclusion about "negative driving force" for dye regeneration. For instance, the standard redox potential of ND-dye in solution is 0.87 V

(by coincidence identical to the M_{redox} of $Cu(tmby)_2^{2+/+}$), but the correctly measured value for ND@TiO_2 is 1.05 V (Fig. 7a). This approach obviously removes the misconception of zero or negative driving force. In any case, the high open-circuit photovoltages of ca. 1.1 V are now achievable in DSSCs. They are well comparable to those of the best performing perovskite solar cells [63].

Applications: perovskite solar cells

Perovskite solar cell (PSC) has demonstrated an unprecedented efficiency jump from 3.8% in the pioneering work in 2009 to the current values exceeding 26% [65], which already attack the Shockley-Queisser limit. PSC is sometimes called the "young sister" of dye-sensitized solar cell to highlight their similar principles [44]. While electrochemistry is a key methodology in DSSCs [44], and the first PSCs were actually pure electrochemical (liquid-junction) devices, this strategy soon became a dead end in PSC [65]. In fact, the key discovery behind the boom of PSC was a replacement of liquid electrolyte solutions by a solid hole-conductor. This finding was made in 2012 independently and almost simultaneously by four prominent scientists in DSSC research, viz. Grätzel and Park [66] and Snaith and Miyasaka [67]. We should note that the replacement of liquid electrolyte solutions by a solid hole-conductor was known long before the "PSC-era." It was actually used in the solid-state DSSC, which was discovered by Grätzel el al. [68] in 1998.

PSC can be schematized as a diode, in which the light absorber (the generic material is $CH_3NH_3PbI_3$ perovskite) is sandwiched between an electron-selective contact (TiO_2, SnO_2, or ZnO) and the hole-conductor capped by a hole-selective contact. Hence, the architecture of PSC can be conceived as a prototypical p-i-n solar cell, in which the intrinsic semiconductor, i.e., perovskite (i), is positioned between the n-/p-selective contacts. The first and still the top successful hole conductor is $N^2,N^2,N^{2'},N^{2'},N^7,N^7,N^{7'},N^{7'}$-octakis(4-methoxyphenyl)-9,9′-spiro-bi[9H-fluorene]-2,2′,7,7′-tetramine (abbreviated *spiro*-OMeTAD) (see Fig. 8a). It was brought to the field from the solid-state DSSCs, but initially from the light-emitting diodes [68]. Another promising hole conductor is CuSCN [65, 69].

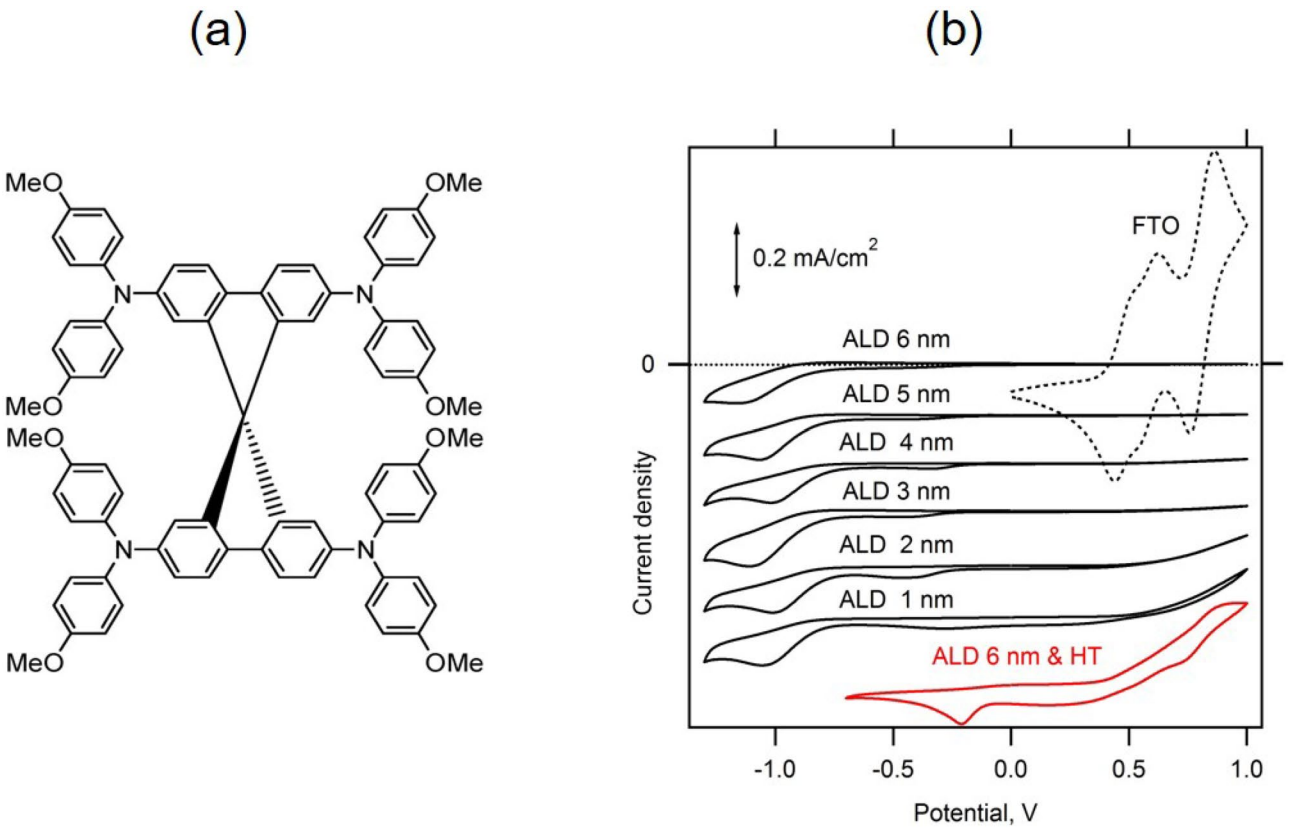

Fig. 8 **a** Molecular formula of *spiro*-OMeTAD. **b** Cyclic voltammogram in dichloromethane electrolyte solution of *spiro*-OMeTAD on FTO electrode (dashed black curve) and on FTO coated with thin-film of TiO_2 made by atomic layer deposition (ALD, the film thickness is indicated in annotations). The red curve is for the 6-nm TiO_2 film after its calcination at 500 °C, 1 h in air. Thermal treatment causes cracking of the film and re-appearance of voltammetric features of *spiro*-OMeTAD. Potentials are referenced against the Ag-wire pseudo-reference electrode. Reprinted with permission from [62]. Copyright (2018) John Wiley and Sons

As in DSSCs, titania thin-film is still the material of the first choice for fabricating the electron-selective layer. In addition to single-phase titania layers, also double layers, e.g., anatase/rutile were employed [18]. The motivation was a better band alignment of CBMs, but this idea is a bit problematic (vide infra). Furthermore, the cited work [18] reports on a curiously opposite anatase/rutile CBM stacking, conflicting most other works [15, 19–21, 52, 53]. The electron-selective (blocking) layers for DSSC/PSC are tested for their pinhole-free texture. This is mandatory not only for Mott-Schottky analyses (see above) but also for preventing the contact of the negative terminal (FTO) with the electrolyte mediator or hole conductor. The *spiro*-OMeTAD can also serve as a suitable redox probe, i.e., an alternative to the common $Fe(CN)_6^{3-/4-}$. Figure 8b demonstrates a perfectly rectifying behavior of ultrathin TiO_2 layers made by atomic layer deposition (ALD). Unfortunately, these layers are sensitive to cracking upon heat treatment [34, 70].

Some authors prefer SnO_2 for the e-selective transport layers in PSC. They do not crack upon calcination [32] and have ca. 100-times larger electron mobility [71]. Also the larger E_{BG} of SnO_2 (Table 1) improves stability against photodegradation under solar light [72]. The quantum dot-SnO_2 provides still larger E_{BG} of ≈4 eV, thanks to quantum-size effect. This is beneficial for improved electron capture and stability [73].

It is tempting to discuss the open-circuit photovoltage of PSC in terms of the electronic band diagrams. More specifically, some authors tried to compare the CBM/VBM of perovskite (e.g., − 3.93/ − 5.49 eV, respectively, for $CH_3NH_3PbI_3$) with the VBM of hole conductor (e.g., − 5.2 eV for *spiro*-OMeTAD) and the CBMs of the electron-selective contacts (TiO_2, SnO_2, or ZnO; Table 1). The motivation was optimization of the PSC by conduction-band engineering of the electron selective layers, either single-phase or double-phase (e.g., TiO_2(A)/TiO_2(R) or TiO_2/SnO_2) [18, 61, 65, 74]. Though the idea looks rational, and works reasonably well in the case of DSSCs (cf. previous chapter and Fig. 7), it is quite questionable in PSCs. In fact, the open-circuit photovoltages of PSCs employing TiO_2, SnO_2, or ZnO as the e-selective contacts are all about the same (around 1.1 V), despite the CBM of SnO_2 is markedly lower [65, 71]. Obviously, there must be other factors, beyond the band alignment, which control the photopotential of PSC.

For instance, the often-ignored interface between the transparent conductive oxide (e.g., FTO) and e-transport layer (TiO_2, SnO_2, ZnO…) deserves attention. Walter et al. [75] investigated the parasitic Schottky junction at this interface, which is responsible for conductance loses (TiO_2 was quite susceptible to this problem). Unfortunately, the discussion requires quantification of the Fermi level misalignment between, e.g., TiO_2 and FTO, which is a thorny issue (cf. Figure 3).

Applications: Li-batteries

SnO_2 and ZnO are attractive materials for the negative electrode of Li-battery, thanks to their large charge capacity. It corresponds to the conversion reactions:

$$SnO_2 + 4Li^+ + 4e^- \rightarrow Sn + 2Li_2O\ [711\ mAh/g] \quad (13a)$$

$$Sn + xLi^+ + xe^- \rightleftarrows Li_xSn\ [\leq 783\ mAh/g;\ x \leq 4.4] \quad (13b)$$

$$ZnO + 2Li^+ + 2e^- \rightleftarrows Zn + Li_2O\ [658\ mAh/g] \quad (13c)$$

$$Zn + xLi^+ + xe^- \rightleftarrows Zn + Li_2O\ [\leq 329\ mAh/g;\ x \leq 1] \quad (13d)$$

The conversion reactions are hardly understood in terms of the electronic band structure. On the other hand, TiO_2 (in all its naturally occurring forms, i.e., anatase, rutile, brookite, and TiO_2(B)) is active in the topotactic Li-accommodation:

$$TiO_2 + x\left(Li^+ + e^-\right) \rightarrow Li_xTiO_2\left[168\ mAh/g\ for\ x = 0.5\right] \quad (14)$$

The coefficient x varied from 0.1 to 1 for different titania phases [76], but x≈0.5 is most often encountered in the literature. At this point, we can make two terminological notes:

1. The accommodation of lithium in host structures is termed either "insertion" or "intercalation" (from the Latin verb *intercalare*, used originally for adding extra month, *mensis intercalaris*, into the Roman calendar). The IUPAC recommendation from 1995 [77] reserved the term "intercalation" for lithium storage in *laminar host structures.* None of TiO_2 polymorphs has layered structure, hence, the term "insertion" is preferable. Nevertheless, the next IUPAC recommendation from 2007 [78] provided softer coding, which allowed the term "intercalation" for *any* one-, two-, or three-dimensional hosts. Hence, the wording "intercalation into TiO_2" is acceptable, though many authors insist traditionally on the term "insertion."
2. The battery community ubiquitously uses the term *anode* for what is properly named the "negative electrode" (and conversely, the term *cathode* for the "positive electrode"). These terms are actually slang words. After all, we teach students that the anode is where the oxidation occurs, and this electrode is negative during *both* charging and discharging, but it is an anode only during the discharge. (At charging it is, technically, a cathode, i.e., a reduction reaction occurs.)

The Li-insertion, like any cathodic dark reaction on n-type semiconductors, proceeds at potentials ≤ V_{fb}, when

the host material is in the accumulation (quasi-metallic) regime. From the known values of V_{fb} in Li-containing aprotic medium (Fig. 3) this prediction is correct, at least qualitatively: the difference in formal potentials of Li-insertion into anatase/rutile is about 0.38 V for single crystal electrodes and about 0.5 V for polycrystalline titania [42, 76, 79, 80]. Nevertheless, the assumption that the Li-insertion into TiO_2 is triggered at V_{fb} is incorrect. In fact, big overvoltages downshift the onset potentials for Li-insertion by hundreds of mV [42, 76, 79, 80].

On the other hand, this reasoning works surprisingly well, if TiO_2 (anatase) is employed as an additive for the cathode of the Li-sulfur battery. Zlamalova et al. [79] confirmed that the reduction of S_8 on anatase starts at 2.1 V vs. Li^+/Li. This agrees perfectly with the V_{fb} measured in the same electrolyte solution, indicating negligible overvoltage of this reaction.

The majority of works on the Li/titania deal with anatase [61, 71, 76, 79–85]. Attention is paid to kinetic analysis [82, 83], distinction of insertion and (pseudo)capacitive phenomena [84], crystal-face specific Li-insertion activity [42], in situ Raman spectroelectrochemistry with isotopic labeling ($^{16/18}O$, $^{6/7}Li$) [85] up to fabrication of anodes for practical Li-ion batteries [76]. It has been long speculated that small particle size of nanocrystalline anatase is responsible for improved kinetics of Li-storage, but Dahlman et al. [82] showed recently that the situation is more complex. According to their study, the Li-insertion rates depend on the applied overpotential, electrolyte concentration, and initial state of charge. Recently, Tetteh et al. [83] reported on fast Li-storage in a 50 nm sized anatase particle. More precisely, the *x*-value of ≈0.3 (Eq. 14) was achieved by cyclic voltammetry at 0.1 V/s scan rate (corresponding to C-rate above 100 C).

Errors by the author: some examples (out of many)

In 1993, I co-authored a textbook "Principles of Electrochemistry" [86], which unfortunately, contains many errors discussed above. More specifically, this book presents: (i) the problematic diagram of electronic bands (p. 398, Fig. 5.59), (ii) the oversimplified model of a semiconductor/electrolyte interface (p. 399, Fig. 5.60), (iii) the wrong scheme of dye-sensitized solar cells with band bending in the semiconductor photoanode (p. 404, Fig. 5.63). In the same year, we reported on quantum-size effects in "anatase nanoparticles" having dimensions as low as ≈1 nm [87]. Since the lattice constant (c) of anatase is ≈0.94 nm, one could ask a provocative question, whether our TiO_2 particle was still a "crystal?".

In 2004, we observed two extra peaks (called S-peaks) in the cyclic voltammograms of Li-insertion into anatase, synthesized by hydrothermal growth, and attributed it to a quantum-size confinement in titania nanosheets [88] or to surface charging in well-organized anatase nanostructures [89]. Both ideas were totally wrong; the correct explanation was that the S-peaks were signatures of a monoclinic phase, TiO_2(B), which we had overlooked [90].

In 2012, we found that the open-circuit photovoltage of a DSSC employing (001)-oriented anatase TiO_2 was by 45 mV larger, than that of the reference cell with ordinary (101)-anatase [91]. The enhancement was attributed to a negative shift in flatband potential. This reasoning was questionable with respect to the poorly defined V_{fb} in nanoporous materials. The story was revisited [92], and the effect was elucidated by differences in lifetime and diffusion coefficients of electrons. Furthermore, we sometimes used the oversimplified Mott-Schottky plot at single frequency for characterization of anatase single crystals [41, 42].

In 2017, we reported on "metal-like" Ta-doped TiO_2 (anatase) exhibiting quasi-reversible cyclic voltammograms of $Fe(CN)_6^{3-/4-}$ and dimethylviologen redox couples like on FTO [81]. This assumption failed for $Ru(bpy)_3^{3+/2+}$, which was idle on a Ta:TiO_2 electrode. Similar behavior was observed for ALD-grown SnO_2. It provided a rectifying (semiconductor-like) interface for $Fe(CN)_6^{3-/4-}$ in the as-received (quasi-amorphous) state, but metal-like electrochemistry after the calcination-driven crystallization; $Ru(bpy)_3^{3+/2+}$ was electrochemically silent at both electrodes [32]. We proposed an explanation based on a ≈0.5 eV downshift of the Fermi level upon thermal crystallization, which was hopefully correct for SnO_2, but hardly applicable for ALD-TiO_2 which did not show any marked changes upon thermal treatment [23]. Hence, our "discovery" of a metallic transparent titania electrode remains elusive.

Conclusions

Some technical and formal ambiguities in semiconductor electrochemistry are outlined in this review. Its principal motivation is *not* the criticism of errors, but to aid students and teachers of electrochemistry. Selected examples of challenging issues are:

(i) Determination of flatband potentials and donor concentrations by Mott-Schottky analysis, particularly for nanotextured materials. Huge spread of literature data of flatband potentials of TiO_2, SnO_2, and ZnO. Unrealistically high concentrations of the majority charge carriers, which can even wrongly predict degenerated semiconductors.

(ii) Calculation of work functions and band edges by DFT and ignoring the effects of sample environment, and/or defects in real crystals.

(iii) Measurement of work functions and band edges by a single experimental technique only (e.g., by photoelectron spectroscopy, Kelvin probe, or by electrochemistry). Disregarding the inherently poor reproducibility of the values from each individual technique.

(iv) Transposition of these problematic data, both theoretical and experimental, into discussions of water splitting, solar fuel generation, solar cells, and Li-ion batteries.

(v) The endless contradictory debate about CBM stacking in titania anatase/rutile and its impact to photocatalysis. The elucidation of synergic effects in mixed-phase photocatalysts (e.g., P25).

(vi) Application of the Gärtner-Butler model for carrier dynamics in a semiconductor photoanode, disregarding, e.g., the gradient of electrochemical potentials as the driving force for e^-/h^+ separation.

(vii) The "superhydrophilicity" in UV-irradiated titania appears to be caused by selective adsorption/photodegradation of airborne carboxylic acids, rather than by structural modifications of the TiO_2 surface.

Epilogue "There are more things in heaven and Earth, Horatio, Than are dreamt of in your philosophy." (Hamlet, 1st act, 5th scene)

Funding Open access publishing supported by the National Technical Library in Prague. This work was supported by the Grant Agency of the Czech Republic (contract No. 22-24138S).

Open Access This article is licensed under a Creative Commons Attribution 4.0 International License, which permits use, sharing, adaptation, distribution and reproduction in any medium or format, as long as you give appropriate credit to the original author(s) and the source, provide a link to the Creative Commons licence, and indicate if changes were made. The images or other third party material in this article are included in the article's Creative Commons licence, unless indicated otherwise in a credit line to the material. If material is not included in the article's Creative Commons licence and your intended use is not permitted by statutory regulation or exceeds the permitted use, you will need to obtain permission directly from the copyright holder. To view a copy of this licence, visit http://creativecommons.org/licenses/by/4.0/.

References

1. Chen X, Selloni A (2014) Introduction: titanium dioxide TiO_2 nanomaterials. Chem Rev 114:9281–9282
2. Hagfeldt A, Vlachopoulos N (2023) Photoelectrochemistry of semiconductors. Jenny Stanford Publ, Singapore
3. Klein A, Albe K, Bein N, Clemens O, Creutz KA, Erhart P, Fredricks M, Ghorbani E, Hofmann JP, Huang BX, Kaiser B, Kolb U, Koruza J, Kübel C, Lohaus KNS, Rödel J, Rohrer J, Rheinheimer W, De Souza RA, Streibel V, Weidenkaff A, Widenmeyer M, Xu BX, Zhang HB (2023) The Fermi energy as common parameter to describe charge compensation mechanisms: a path to Fermi level engineering of oxide electroceramics. J Electroceram: https://doi.org/10.1007/s10832-023-00324-y
4. Kavan L (2010) Titania in diverse forms as substrates, in: K. Kalyanasundaram (ed.), Dye-sensitized solar cells, CRC Press Taylor & Francis, Boca Raton: pp. 45–81
5. Buckeridge J, Butler KT, Catlow CRA, Logsdail AJ, Scanlon DO, Shevlin SA, Woodley SM, Sokol AA, Walsh A (2015) Polymorph engineering of TiO_2 demonstrating how absolute reference potentials are determined by local coordination. Chem Mater 27:3844–3851
6. Gleria M, Memming R (1975) Charge transfer processes at large band gap semiconductor electrodes: reactions at SiC-electrodes. J Electroanal Chem 65:163–175
7. Fujishima A, Honda K (1972) Electrochemical photolysis of water at a semiconductor electrode. Nature 238:37–38
8. Boddy PJ (1968) Oxygen evolution on semiconducting TiO_2. J Electrochem Soc 115:199–203
9. Ohtani B (2014) Revisiting the original works related to titania photocatalysis. Electrochemistry 82:414–425
10. Trasatti S (1986) The absolute electrode potential: an explanatory note. Pure Appl Chem 58:955–966
11. Ramette RW (1987) Outmoded terminology: the normal hydrogen electrode. J Chem Educ 64:885–885
12. Jerkiewicz G (2020) Standard and reversible hydrogen electrodes: theory, design, operation, and applications. ACS Catal 10:8409–8417
13. Bisquert J, Cendula P, Bertoluzzi L, Gimenez S (2014) Energy diagram of semiconductor/electrolyte junctions. J Phys Chem Lett 5:205–207
14. Krysova H, Mansfeldova V, Tarabkova H, Pisarikova A, Hubicka Z, Kavan L (2023) High-quality dense ZnO thin-films: work function and photo/electrochemical properties. J Solid State Electrochem. https://doi.org/10.1007/s10008-023-05766-6
15. Mansfeldova V, Zlamalova M, Tarabkova H, Janda P, Vorokhta M, Piliai L, Kavan L (2021) Work function of TiO_2 (anatase, rutile, and brookite) single crystals: effects of the environment. J Phys Chem C 125:1902–1912
16. Patel MY, Mortelliti MJ, Dempsey JL (2022) A compendium and meta-analysis of flatband potentials for TiO_2, ZnO, and SnO_2 semiconductors in aqueous media. Chem Phys Rev 3:011303
17. Kashiwaya S, Morasch J, Toupance T, Jaegermann W, Klein A (2018) The work function of TiO_2. Surfaces 1:73–89
18. Zhu Y, Deng K, Sun H, Gu B, Lu H, Cao F, Xiong J, Li L (2018) TiO_2 phase junction electron transport layer boosts efficiency of planar perovskite solar cells. Adv Sci 5:1700614
19. Mi Y, Weng Y (2015) Band alignment and controllable electron migration between rutile and anatase TiO_2. Sci Rep 5:11482
20. Zhang D, Dong S (2019) Challenges in band alignment between semiconducting materials: a case of rutile and anatase TiO_2. Prog Nat Sci Mater Int 29:277–284
21. Scanlon DO, Dunnill CW, Buckeridge J, Shevlin SA, Logsdail AJ, Woodley SM, Catlow CRA, Powell MJ, Palgrave RG, Parkin IP, Watson GW, Keal TW, Sherwood P, Walsh A, Sokol AA (2013) Band alignment of rutile and anatase TiO_2. Nat Mater 12:798–801
22. Deak P, Kullgren J, Aradi B, Frauenheim T, Kavan L (2016) Water splitting and the band edge positions of TiO_2. Electrochim Acta 199:27–34
23. Zlamalova M, Mansfeldova V, Tarabkova H, Krysova H, Kavan L (2023) Variable work function of semiconducting thin-film oxide electrodes: a case study of SnO_2 and TiO_2. J Solid State Electrochem 27:1935–1943
24. Zhang B, Wang Z, Huang B, Zhang X, Qin X, Li H, Dai Y, Li Y (2016) Anisotropic photoelectrochemical (PEC) performances of ZnO single-crystalline photoanode: effect of internal electrostatic fields on the separation of photogenerated charge carriers during PEC water splitting. Chem Mater 28:6613–6620
25. Kavan L, Zlamalova M, Mansfeldova V, Krysova H, Tarabkova H, Pitňa Lásková B (2023) Interplay of band energetics and photo/electro/chemical activity of SnO_2 thin films. Monatsh Chem. https://doi.org/10.1007/s00706-023-03145-5

26. Krysova H, Zlamalova M, Tarabkova H, Jirkovsky J, Frank O, Kohout M, Kavan L (2019) Rutile TiO_2 thin film electrodes with excellent blocking function and optical transparency. Electrochim Acta 321:134685
27. Beranek R (2011) Photoelectrochemical methods for the determination of the band edge positions in TiO_2-based nanomaterials. Adv Phys Chem 786759–78675920
28. Lee SF, Jimenez-Relinque E, Martinez I, Castellote M (2023) Effects of Mott-Schottky frequency selection and other controlling factors on flat-band potential and band-edge position determination of TiO_2. Catalysts 13:1000
29. Kavan L, Vlckova-Zivcova Z, Petrak V, Frank O, Janda P, Tarabkova H, Nesladek M, Mortet V (2015) Boron-doped diamond electrodes: electrochemical, atomic force microscopy and Raman study towards corrosion-modifications at nanoscale. Electrochim Acta 179:626–636
30. Hankin A, Bedoya-Lora FE, Alexander JC, Regoutz A, Kelsall GH (2019) Flat band potential determination: avoiding the pitfalls. J Mater Chem A 7:26162–26176
31. Gateman SM, Gharbi O, Gomes de Melo H, Ngo K, Turmine M, Vivier V (2022) On the use of a constant phase element (CPE) in electrochemistry. Current Opinion Electrochem 36:101133
32. Kavan L, Steier L, Grätzel M (2017) Ultrathin buffer layers of SnO_2 by atomic layer deposition: perfect blocking function and thermal stability. J Phys Chem C 121:342–350
33. Kavan L, Vlckova-Zivcova Z, Zlamalova M, Zakeeruddin SM, Grätzel M (2020) Electron-selective layers for dye-sensitized solar cells based on TiO_2 and SnO_2. J Phys Chem C 124:6512–6521
34. Kavan L, Tetreault N, Moehl T, Grätzel M (2014) Electrochemical characterization of TiO_2 blocking layers for dye sensitized solar cells. J Phys Chem C 118:16408–16418
35. Michaels H, Freitag M (2022) Assessment of TiO_2 blocking layers for Cu(II/I)-electrolyte dye-sensitized solar cells by electrochemical impedance spectroscopy. ACS Appl Energy Mater 5:1933–1941
36. Bisquert J, Garcia-Belmonte G, Fabregat-Santiago F (1999) Modelling the electric potential distribution in the dark in nanoporous semiconductor electrodes. J Solid State Electrochem 3:337–347
37. Peter LM, Gurudayal WLH, Abdi FF (2018) Understanding the role of nanostructuring in photoelectrode performance for light-driven water splitting. J Electroanal Chem 819:447–458
38. Sivula K (2021) Mott-Schottky analysis of photoelectrodes: sanity checks are needed. ACS Energy Lett 6:2549–2551
39. Quarto FD, Franco FD, Miraghaei S, Santamaria M, La Mantia F (2017) The amorphous semiconductor schottky barrier approach to study the electronic properties of anodic films on Ti. J Electrochem Soc 164:C516–C525
40. Setvin M, Daniel B, Mansfeldova V, Kavan L, Scheiber P, Fidler M, Schmid M, Diebold U (2014) Surface preparation of TiO_2 anatase (101): pitfalls and how to avoid them. Surf Sci 626:61–67
41. Kavan L, Grätzel M, Gilbert SE, Klemenz C, Scheel HJ (1996) Electrochemical and photoelectrochemical investigation of single-crystal anatase. J Am Chem Soc 118:6716–6723
42. Hengerer R, Kavan L, Krtil P, Grätzel M (2000) Orientation dependence of charge transfer processes on TiO_2 (anatase) single crystal. J Electrochem Soc 147:1467–1472
43. Hagfeldt A, Boschloo G, Sun L, Kloo L, Pettersson H (2010) Dye-sensitized solar cells. Chem Rev 110:6595–6663
44. Kavan L (2017) Electrochemistry and dye-sensitized solar cells. Curr Opinion Electrochem 2:88–96
45. Berger T, Monllor-Setoca D, Jankulovska M, Lana-Villarreal T, Gomez R (2012) The electrochemistry of nanostructured titanium dioxide electrodes. ChemPhysChem 13:2824–2875
46. Di Liberto G, Morales-Garcia A, Bromley ST (2022) An unconstrained approach to systematic structural and energetic screening of materials interfaces. Nat Commun 13:6236
47. Bayani A, Gebhardt J, Elsasser C (2023) Electronic bulk and surface properties of titanium dioxide studied by DFT-1/2. Langmuir 39:14922–14934
48. Ko KC, Bromley ST, Lee JY, Illas F (2017) Size-dependent level alignment between rutile and anatase TiO_2 nanoparticles: implications for photocatalysis. J Phys Chem Lett 8:5593–5598
49. Zhang W, Yan D, Appavoo K, Cen J, Wu Q, Orlov A, Sfeir MY, Liu M (2017) Unravelling photocarrier dynamics beyond the space charge region for photoelectrochemical water splitting. Chem Mater 29:4036–4043
50. Baldini E, Chiodo L, Dominguez A, Palummo M, Moser S, Yazdi-Rizi M, Aubock G, Mallett BPP, Berger H, Magrez A, Bernhard C, Grioni M, Rubio A, Chergui M (2017) Strongly bound excitons in anatase TiO_2 single crystals and nanoparticles. Nat Commun 8:13
51. Schleuning M, Ahmet IY, van de Krol R, May MM (2022) The role of selective contacts and built-in field for charge separation and transport in photoelectrochemical devices. Sust Energy Fuels 6:3701–3716
52. Yaemsunthorn K, Kobielusz M, Macyk W (2021) TiO_2 with tunable anatase-to-rutile nanoparticles ratios: how does the photoactivity depend on the phase composition and the nature of photocatalytic reaction? ACS Appl Nano Mater 4:633–643
53. Nosaka Y, Nosaka AY (2016) Reconsideration of intrinsic band alignments within anatase and rutile TiO_2. J Phys Chem Lett 7:431–434
54. Sun X, Chang Y, Cheng Y, Feng Y, Zhang H (2018) Band alignment-driven oxidative injury to the skin by anatase/rutile mixed-phase titanium dioxide nanoparticles under sunlight exposure. Toxicol Sci 164:300–312
55. Schneider J, Matsuoka M, Takeuchi M, Zhang J, Horiuchi Y, Anpo M, Bahnemann DW (2014) Understanding TiO_2 photocatalysis: mechanisms and materials. Chem Rev 114:9919–9986
56. Balajka J, Hines MA, DeBenedetti WJI, Komora M, Pavelec J, Schmid M, Diebold U (2018) High-affinity adsorption leads to molecularly ordered interfaces on TiO_2 in air and solution. Science 361:786–789
57. O'Regan B, Grätzel M (1991) A low-cost high efficiency solar cell based on dye-sensitized titanium dioxide. Nature 353:737–740
58. Ren Y, Zhang D, Suo J, Cao Y, Eickemeyer FT, Vlachopoulos N, Zakeeruddin SM, Hagfeldt A, Gratzel M (2023) Hydroxamic acid pre-adsorption raises the efficiency of cosensitized solar cells. Nature 613:60–65
59. Saygili Y, Soderberg M, Pellet N, Giordano F, Cao Y, Munoz-Garcia AB, Zakeeruddin SM, Vlachopoulos N, Pavone M, Boschloo G, Kavan L, Moser JE, Grätzel M, Hagfeldt A, Freitag M (2016) Copper bipyridyl redox mediators for dye-sensitized solar cells with high photovoltage. J Am Chem Soc 138:15087–15096
60. Ferdowsi P, Saygili Y, Zakeeruddin SM, Mokhtari J, Grätzel M, Hagfeldt A, Kavan L (2018) Alternative bases to 4-tert-butylpyridine for dye-sensitized solar cells employing copper redox mediator. Electrochim Acta 265:194–201
61. Kavan L (2019) Conduction band engineering in semiconducting oxides (TiO_2, SnO_2): applications in perovskite photovoltaics and beyond. Catal Today 328:50–56
62. Ferdowsi P, Saygili Y, Zhang W, Edvinson T, Kavan L, Mokhtari J, Zakeeruddin SM, Grätzel M, Hagfeldt A (2018) Molecular design of efficient organic d-a-pi-a dye featuring triphenylamine as donor fragment for application in dye-sensitized solar cells. ChemSusChem 11:494–502
63. Zhang W, Wu Y, Bahng HW, Cao Y, Chenyi Y, Saygili Y, Luo J, Liu Y, Kavan L, Moser JE, Hagfeldt A, Tian H, Zakeeruddin SM, Zhu WH, Grätzel M (2018) Comprehensive control of voltage loss enables 11.7% efficient solid-state dye-sensitized solar cells. Energy Environ Sci 11:1179–1187
64. Yum J-H, Baranoff E, Kessler F, Moehl T, Ahmad S, Bessho T, Marchioro A, Ghadiri E, Moser JE, Nazeeruddin MK, Grätzel M

(2012) Rationally designed cobalt complexes as redox shuttle for dye-sensitized solar cells to exceed 1000 mV. Nature Comm 3:631–6318
65. Jena AK, Kulkarni A, Miyasaka T (2019) Halide perovskite photovoltaics: background, status, and future prospects. Chem Rev 119:3036–3103
66. Kim HS, Lee CR, Im JH, Lee K, Moehl T, Marchioro A, Moon SJ, Humphry-Baker R, Yum J-H, Moser JE, Grätzel M, Park NG (2012) Lead iodide perovskite sensitized all-solid-state submicron thin film mesoscopic solar cell with efficiency exceeding 9%. Sci Rep 2:591
67. Lee MM, Teuscher J, Miyasaka T, Murakami TN, Snaith HJ (2012) Efficient hybrid solar cell based on meso-superstructured organometal halide perovskite. Science 338:643–647
68. Bach U, Lupo D, Comte P, Moser J, Weissortel F, Salbeck J, Spreitzer H, Grätzel M (1998) Solid-state dye-sensitized mesoporous TiO_2 solar cells with high photon-to-electron conversion efficiencies. Nature 395:583–585
69. Kavan L, Vlckova-Zivcova Z, Hubik P, Arora N, Dar MI, Zakeeruddin SM, Grätzel M (2019) Electrochemical characterization of CuSCN hole-extracting thin films for perovskite photovoltaics. ACS Appl Energy Mater 2:4264–4273
70. Moehl T, Suh J, Severy L, Wick-Joliat R, Tilley SD (2017) Investigation of (leaky) ALD TiO_2 protection layers for water-splitting photoelectrodes. ACS Appl Mat Interfaces 9:43614–43622
71. Jiang Q, Zhang L, Wang H, Yang X, Meng J, Liu H, Yin Z, Wu J, Zhang X, You J (2016) Enhanced electron extraction using SnO_2 for high-efficiency planar-structure $HC(NH_2)_2PbI_3$-based perovskite solar cells. Nature Energy 2: 16177
72. Ma F, Zhao Y, Qu ZH, You JB (2023) Developments of highly efficient perovskite solar cells. Acc Mater Res 4:716–725
73. Kim M, Jeong J, Lu H, Lee TK, Eickemeyer FT, Liu Y, Choi IW, Choi SJ, Jo Y, Kim HB, Mo SI, Kim YK, Lee H, An NG, Cho S, Tress WR, Zakeeruddin SM, Hagfeldt A, Kim JY, Gratzel M, Kim DS (2022) Conformal quantum dot-SnO_2 layers as electron transporters for efficient perovskite solar cells. Science 375:302–306
74. Lachore WL, Andoshe DM, Mekonnen MA, Hone FG (2021) Recent progress in electron transport bilayer for efficient and low-cost perovskite solar cells: a review. J Solid State Electrochem 26:295–311
75. Walter D, Peng J, Weber K, Catchpole KR, White TP (2022) Performance limitations imposed by the TCO heterojunction in high efficiency perovskite solar cells. Energy Environ Sci 15:5202–5216
76. Aravindan V, Lee YS, Yazami R, Madhavi S (2015) TiO_2 polymorphs in "rocking-chair" Li-ion batteries. Mater Today 18:345–351
77. Moss GP, Smith PAS, Tavernier D (1995) Glossary of class names of organic compounds. Pure Appl Chem 67:1307–1375
78. Aleman J, Chadwick AV, He J, Hess M, Horie K, Jones RG, Kratochvil P, Meisel I, Mita I, Moad G, Penczek S, Stepto RFT (2007) Definition of terms relating to the structure and properties. Pure Appl Chem 79:1801–1829
79. Zlamalova M, Pitna Laskova B, Vinarcikova M, Zukalova M, Kavan L (2022) Inherent electrochemical activity of TiO_2 (anatase, rutile) enhances the charge capacity of cathodes of lithium-sulfur batteries. J Solid State Electrochem 26:639–647
80. Kavan L (2014) Lithium insertion into TiO_2 (anatase): electrochemistry, raman spectroscopy, and isotope labeling. J Solid State Electrochem 18:2297–2306
81. Krysova H, Mazzolini P, Casari CS, Russo V, Li Bassi A, Kavan L (2017) Electrochemical properties of transparent conducting films of tantalum-doped titanium dioxide. Electrochim Acta 232:44–53
82. Dahlman CJ, Heo S, Zhang Y, Reimnitz LC, He D, Tang M, Milliron DJ (2021) Dynamics of lithium insertion in electrochromic titanium dioxide nanocrystal ensembles. J Am Chem Soc 143:8278–8294
83. Tetteh EB, Valavanis D, Daviddi E, Xu X, Santana Santos C, Ventosa E, Martin-Yerga D, Schuhmann W, Unwin PR (2023) Fast Li-ion storage and dynamics in TiO_2 nanoparticle clusters probed by smart scanning electrochemical cell microscopy. Angew Chem Int Ed Engl 62:e202214493
84. Laskova B, Zukalova M, Zukal A, Bousa M, Kavan L (2014) Capacitive contribution to Li-storage in TiO_2(B) and TiO_2 (anatase). J Power Sourc 246:103–109
85. Laskova B, Frank O, Zukalova M, Bousa M, Dracinsky M, Kavan L (2013) Lithium inserion into titanium dioxide (anatase): a Raman study with 16/18-O and 6/7-Li labeling. Chem Mater 25:3710–3717
86. Koryta J, Dvořák J, Kavan L (1993) Principles of electrochemistry, 2nd edn. J. Wiley, Chichester
87. Kavan L, Stoto T, Grätzel M, Fitzmaurice D, Shklover V (1993) Quantum size effects in thin semiconducting TiO_2 layers prepared by anodic oxidative hydrolysis of $TiCl_3$. J Phys Chem 97:9493–9498
88. Kavan L, Kalbac M, Zukalova M, Exnar I, Lorenzen V, Nesper R, Grätzel M (2004) Lithium storage in nanostructured TiO_2 made by hydrothermal growth. Chem Mater 16:477–485
89. Kavan L, Rathousky J, Grätzel M, Shklover V, Zukal A (2001) Mesoporous thin film TiO_2 electrodes. Micropor Mesopor Mater 44–45:653–659
90. Zukalova M, Kalbac M, Kavan L, Exnar I, Grätzel M (2005) Pseudocapacitive lithium storage in TiO_2(B). Chem Mater 17:1248–1255
91. Laskova B, Zukalova M, Kavan L, Chou A, Liska P, Wei Z, Bin L, Kubat P, Ghadiri E, Moser JE, Grätzel M (2012) Voltage enhancement in dye-sensitized solar cell using (001)-oriented anatase TiO_2 nanosheets. J Solid State Electrochem 16:2993–3001
92. Laskova B, Moehl T, Kavan L, Zukalova M, Liu X, Yella A, Comte P, Zukal A, Nazeeruddin MK, Grätzel M (2015) Electron kinetics in dye sensitized solar cells employing anatase with (101) and (001) facets. Electrochim Acta 160:296–305
93. Zandi O, Schon AR, Hajibabaei H, Hamann TW (2016) Enhanced charge separation and collection in high-performance electrodeposited hematite films. Chem Mater 28:765–771

Publisher's Note Springer Nature remains neutral with regard to jurisdictional claims in published maps and institutional affiliations.

Ladislav Kavan is a senior scientist at the J. Heyrovsky Institute of Physical Chemistry, Czech Academy of Sciences, and professor of inorganic chemistry at the Faculty of Science, Charles University, Prague, Czech Republic. He was a guest scientist at the Fritz Haber Institute, Berlin, Germany; at the University of Gunma, Kiryu, Japan; and at the Institute of Solid State and Materials Research, Dresden, Germany. He spent many research stays at the Swiss Federal Institute of Technology, Lausanne, Switzerland (EPFL), where, since 1988, he has been a visiting professor of physical chemistry. Ladislav Kavan has enjoyed fruitful collaborations with many colleagues, but three names should be highlighted (in alphabetical order): František P. Dousek (19 joint publications focused on electrochemical carbon), Lothar Dunsch (66 joint publications mainly related to conducting polymers and spectroelectrochemistry of nanocarbons), and Michael Grätzel (59 joint publications on oxide semiconductors, dye-sensitized solar cells, and Li-batteries). Kavan has received nine European grants (FP5-FP7, H2020) supporting research in photocatalysis, photovoltaics, and nanocarbons (e.g., the Graphene Flagship). He is a holder of the Award of the Czech Academy of Sciences for excellent results of great scientific impact

(2008), the František Běhounek prize for promoting Czech Republic and science in European research area (2017), the silver medal of the Faculty of Science, Charles University (2019), and the Metrohm's award for lifelong contribution to the development of electroanalytical chemistry (2021). Kavan's work has been cited over 18,000 times, and his H-index is 61.